Hyeon et al. *Microsystems & Nanoengineering* (2026)12:128
https://doi.org/10.1038/s41378-026-01188-2

Microsystems & Nanoengineering
www.nature.com/micronano

ARTICLE Open Access

Multifunctional bilayer radiative cooling dressing for regenerative wound healing under heat stress

Changhwan Hyeon[1], Han Lee[2], Woo-Seung Kim[3], So-Min Kim[3], Ki-Ju Kwon[3], Juhoon Baek[4], Minkyung Kim[4], Ki-Jong Rhee[3], Sunghee Hyun[2]✉ and Dasol Lee[1]✉

Abstract

Wound healing is influenced by local temperature. Sunlight-induced heating elevates wound temperature, which in turn exacerbates inflammation and infection risks, ultimately delaying regeneration. Despite this critical challenge, current dressings lack any capability for thermal protection. We present a bilayer radiative cooling dressing designed for passive cooling, antibacterial, and antioxidative protection. The top radiative cooling layer is a polyvinyl alcohol matrix with silicon dioxide nanoparticles and eugenol, while the bottom layer contains C-phycocyanin, a natural antioxidant and antibacterial agent. This dressing achieved a solar reflectance of 0.92 (0.3–2.5 μm) and thermal emissivity of 0.92 (8–13 μm), allowing effective heat dissipation. Under outdoor conditions, it maintained surface temperatures up to 15.2 °C below ambient. In a murine full-thickness wound model exposed to simulated sunlight, the dressing suppressed excessive heating (<40 °C) and enhanced repair, achieving 90 ± 2% wound contraction, nearly twice that of a commercial adhesive bandage (47.97 ± 3.45%). These findings integrate passive radiative cooling with antioxidative and antibacterial agent delivery, offering thermal protection and accelerated regenerative healing under heat stress conditions.

Introduction

As the largest organ in the human body, skin is the primary barrier against physical trauma and microbial invasion[1–4]. External injuries, including abrasions, lacerations, and burns, require rapid and coordinated tissue repair, typically proceeding through hemostasis, inflammation, proliferation, and remodeling[5–7]. However, this process is strongly influenced by environmental factors such as temperature, ultraviolet (UV) exposure, humidity[8–12].

Outdoors, direct sunlight can rapidly increase the local temperature of a wound, triggering oxidative stress, amplifying inflammation, and increasing susceptibility to infection[13–15]. Such disruptions substantially delay tissue regeneration[16–19]. Numerous clinical and preclinical studies have shown that maintaining normothermic conditions promotes cell migration, angiogenesis, and tissue remodeling[20–22]. However, thermal regulation alone is insufficient to overcome the multifactorial challenges of wound healing, particularly under oxidative stress and bacterial loads[23–25]. Therefore, simultaneous temperature reduction and delivery of antibacterial and antioxidative agents are important to reestablish physiological balance and accelerate healing, especially in high-temperature outdoor environments.

Despite their widespread clinical use, conventional dressings such as gauze, hydrocolloids, and commercial adhesive bandages (CAB) are limited to moisture retention and physical protection[26–28]. They lack the ability to block solar radiation, particularly UV and near-infrared (NIR) wavelengths, or to dissipate heat produced by sun exposure[29–31]. Notably, even brief exposure to sunlight can increase wound surface temperatures to over 40 °C (Supplementary Fig. S1c), exacerbating inflammation, promoting infection, and elevating the risk of abnormal scar formation[32,33]. In addition, conventional dressings typically do not deliver therapeutic agents, such as

Correspondence: Sunghee Hyun (hyunsh@eulji.ac.kr) or
Dasol Lee (dasol@yonsei.ac.kr)
[1]Department of Biomedical Engineering, Yonsei University, Wonju 26493, Republic of Korea
[2]Department of Biomedical Laboratory Science, Graduate School, Eulji University, Uijeongbu 11759, Republic of Korea
Full list of author information is available at the end of the article

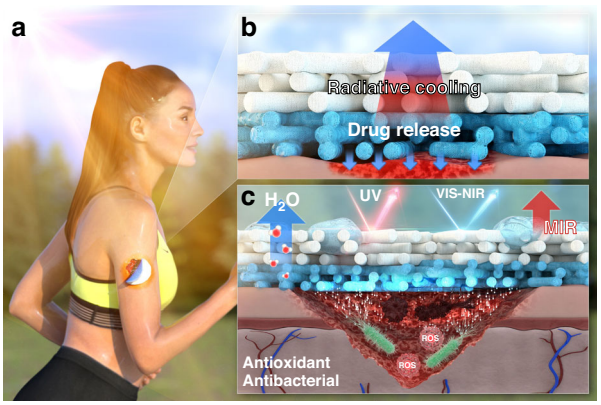

Fig. 1 RCD structure and mechanism for regulating local wound microenvironment. a Schematic of a radiative cooling dressing (RCD) applied to a wound site under sunlight. **b** Cross-section of the RCD bilayer comprised of a white radiative cooling (RC) top layer and blue drug-loaded underlayer. **c** The RC layer reduces local temperature by reflecting solar radiation (UV–VIS–NIR) and emitting heat through the MIR atmospheric window (AW), while its porous nanofibrous structure enables water vapor transmission but blocks liquid water. The C-phycocyanin (C-PC)-loaded bottom layer provides antioxidant and antibacterial functions

antibacterial or antioxidant compounds, directly to the wound, offering no active contribution to healing[34,35].

To overcome these limitations, dressings must go beyond simple protection by integrating solar reflection, thermal regulation, and therapeutic functions. In this context, daytime radiative cooling (RC) has emerged as a promising strategy to enable sub-ambient surface temperature regulation under direct sunlight without external energy input[36–38]. RC works by reflecting solar radiation in the 0.3–2.5 μm range and emitting thermal radiation through the atmospheric window (AW) in the 8–13 μm range, enabling heat dissipation to outer space[39–41]. This principle has been widely applied to buildings, vehicles, electronic devices, and textiles[42–45]. Also, recent work has demonstrated that applying RC to wound dressings can suppress excessive skin heating and thereby promote tissue regeneration[46]. However, this approach was confined to temperature reduction at the wound surface and did not include drug or bioactive delivery functions relevant to healing under heat stress.

Building on this concept, we developed a bilayer radiative cooling dressing (RCD) comprising a top RC layer and a drug-loaded underlayer (Supplementary Fig. S2). The RC layer, composed of a polyvinyl alcohol (PVA) matrix incorporating silicon dioxide (SiO_2) nanoparticles and eugenol (EO) for water-repellent properties, provides high solar reflectance and mid-infrared emissivity within the AW to limit heat accumulation under sunlight. The drug-loaded layer incorporates C-phycocyanin (C-PC), a marine-derived pigment with antioxidant and antibacterial properties, enabling sustained release to mitigate oxidative stress and bacterial infection. By integrating these two layers, the RCD provided effective cooling while maintaining a favorable wound microenvironment that mitigated thermal stress, reduced inflammation, and supported tissue regeneration. This multifunctional design positions RCD as a promising platform for next-generation wound management, integrating thermal protection, antibacterial activity, and antioxidative therapy to address the multifactorial challenges of healing under outdoor thermal stress (Fig. 1a).

Results

RCD was designed as a bilayer system integrating RC with antioxidative and antibacterial treatment (Fig. 1b). The RC layer reduced solar-induced heat buildup through reflection of sunlight and mid-infrared emission, thereby providing a cooling effect, while the drug-loaded layer enabled sustained delivery of bioactive compounds to stabilize the wound microenvironment under heat stress.

The RC layer was fabricated from a PVA[47–49] matrix containing SiO_2 nanoparticles and EO. The refractive-index contrast between SiO_2 (refractive index, $n \approx 1.45$) and PVA ($n \approx 1.55$) gives rise to Mie scattering, enhancing broadband solar reflectance[50,51], while the wide bandgap of SiO_2 ($Eg \approx 9$ eV) prevented absorption of visible (VIS)–NIR photons (1.5–3 eV), thereby minimizing parasitic heating[52,53]. Vibrational modes associated with Si–O–Si and C–O bonds lie within the AW, enabling phonon–polariton–mediated emission and thereby enhancing mid-infrared emissivity[54]. EO, a hydrophobic phenolic compound derived from clove oil, imparted water repellency by reducing surface energy, thereby maintaining the stability of the fibrous RC layer under perspiration and external wetting[55–57]. The drug-loaded layer comprised a PVA matrix containing C-PC, which exhibits intrinsic antioxidative and antibacterial activity and enabled sustained release at the wound site[58,59]. Upon release, C-PC scavenges reactive oxygen species and promotes fibroblast proliferation and collagen deposition, consistent with anti-inflammatory activity[60–62].

These structural features established distinct functional roles for the two layers (Fig. 1c): the RC layer governed broadband solar reflectance together with strong mid-infrared emissivity within the AW, while the drug-loaded layer supplied continuous antioxidative and antibacterial action. Overall, the bilayer design combines RC with sustained C-PC delivery, providing thermal protection and supporting accelerated healing under heat stress.

Spectral measurements were first conducted on the RC layer, using PVA/EO and PVA/EO/SiO_2 composites containing SiO_2 nanoparticles (20–30 nm) at varying loadings (Fig. 2a). Increasing SiO_2 content resulted in a monotonic enhancement of both solar reflectance and

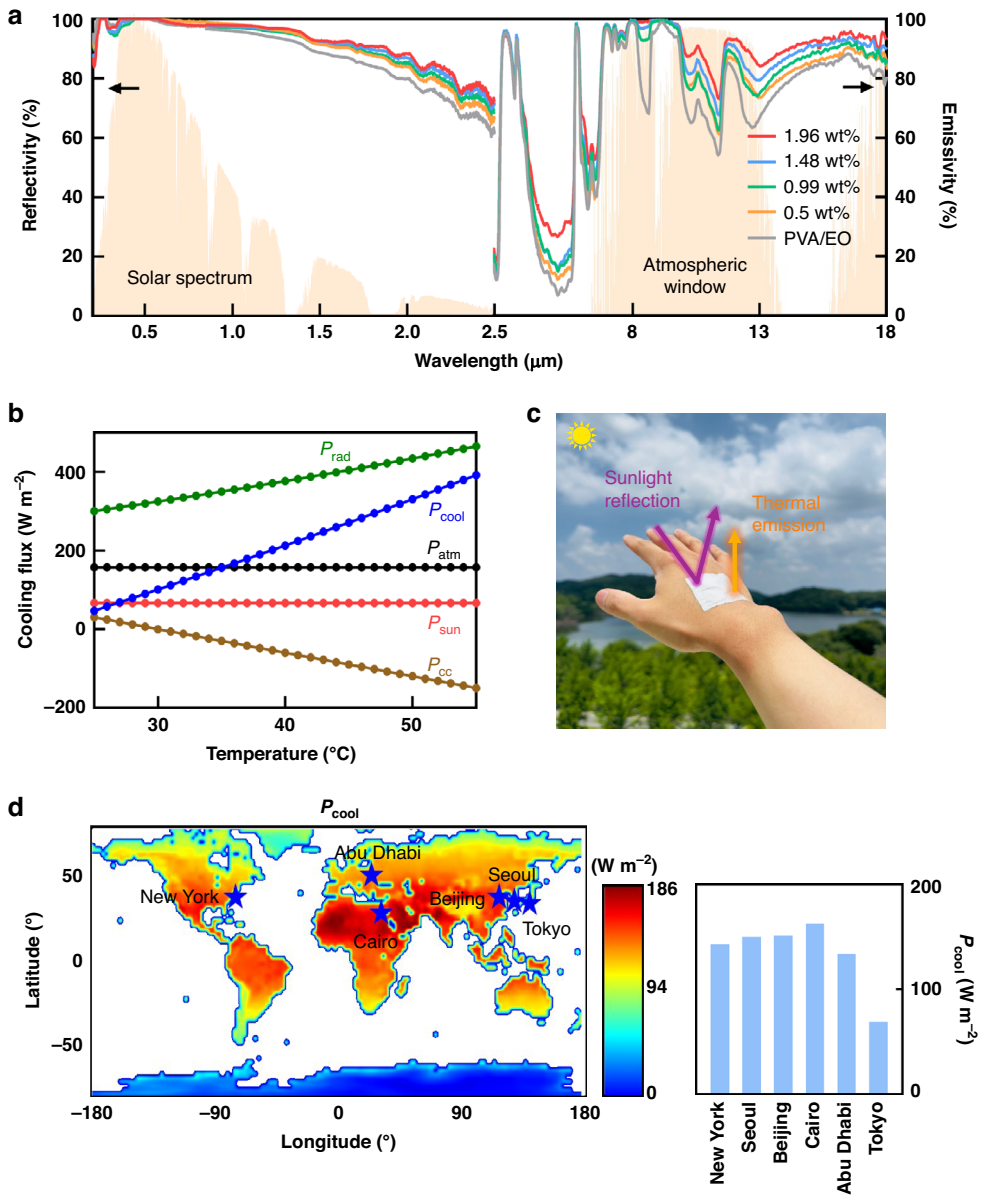

Fig. 2 Optical properties and simulated RC performance of the RCD. a Reflectivity (left, 0.3–2.5 μm) and emissivity (right, 2.5–18 μm) spectra of the RC top layer across the solar spectrum and AW. Samples consisted of PVA/eugenol (EO) and PVA/EO/SiO_2 composites with SiO_2 concentrations of 0.5, 0.99, 1.48, and 1.96 wt%. **b** Simulated cooling flux (P_{cool}) and its thermodynamic components (P_{rad}, P_{sun}, P_{atm}, and P_{cc}) computed under standard ambient conditions. **c** Photograph of fabricated RCD applied to human skin. **d** Global RC potential of the RCD visualized by P_{cool} mapping from the NASA POWER database with representative values for six cities

mid-infrared emissivity. At 1.96 wt% SiO_2, the RC layer achieved an average solar reflectance of 92% and an emissivity of 92% within the AW. These improvements were driven by bandgap-mediated suppression of solar absorption, Mie scattering from the PVA/SiO_2 refractive index contrast, and phonon–polariton resonances that facilitate thermal emission. Importantly, drug-loaded underlayer did not compromise these optical properties. The drug-loaded layer itself exhibited 91% AW emissivity and contributed to maintaining the optical performance of the RC layer (Supplementary Fig. S3). As a result, the complete bilayer RCD with 1.96 wt% SiO_2 maintained a solar reflectance of 92% and AW emissivity of 92% (Supplementary Fig. S4). To avoid aggregation-induced degradation of reflectance, the SiO_2 loading was limited to 1.96 wt%[63].

To quantify cooling performance, numerical simulations were performed using ViBA Rad[64] (Fig. 2b). Net

cooling power (P_{cool}) was quantified by considering radiative emission, solar absorption, atmospheric back-radiation, and nonradiative heat exchange, as detailed in Supplementary Note S1. Under standard ambient conditions ($T_a = 303$ K, $h_{cc} = 6$ $Wm^{-2}K^{-1}$), the RCD exhibited positive P_{cool} values across a surface temperature range of 298–328 K (Fig. 2b). High solar reflectance results in white color and minimizes P_{sun}, whereas P_{rad} increases with temperature, dominating the net cooling flux (Fig. 2c). This indicates robust passive cooling capacity without reliance on external power input.

To evaluate global applicability, RC potential was simulated using experimentally measured spectra and atmospheric data from the NASA POWER database (Fig. 2d), with consistently positive values across diverse climatic regions. Notably, extreme environments such as Cairo and Abu Dhabi exhibited the highest cooling fluxes, with Cairo reaching 168 Wm^2. All six representative cities (New York, Cairo, Abu Dhabi, Beijing, Seoul, and Tokyo) demonstrated favorable cooling performance, highlighting the RCD's potential as a broadly deployable thermal management solution that maintains effective solar reflection and radiative heat dissipation across diverse climatic regions.

To validate RCD in dynamic wound environments, we measured its structural configuration, mechanical adaptability, and functional properties (Fig. 3). The RCD exhibited flexibility sufficient to provide intimate contact with curved anatomical sites such as finger joints, without structural failure or delamination (Fig. 3a). In addition to its flexibility, RCD displayed spontaneous adhesion to moist skin, driven by the inherent hydrophilicity and swelling tendency of the drug-loaded layer. This adhesive feature eliminates the need for external tape or glue, which may cause chemical irritation or disruption of newly formed tissue during removal[65].

The RC layer exhibited a highly porous nanofibrous network in which SiO_2 nanoparticles were randomly distributed within the PVA matrix (Fig. 3b). The average fiber diameter was 288 ± 42 nm (Fig. 3c), while the drug-loaded underlayer showed finer fibers (200 ± 41 nm, Fig. 3d–e), indicating a high surface area suitable for efficient drug loading and sustained release.

In the RC layer, bead-like structures were observed along the fiber axis (Fig. 3b), whereas pure PVA fibers (Supplementary Fig. S5e) prepared under identical electrospinning conditions showed no such morphology. This feature is attributed to the partial aggregation of SiO_2 nanoparticles during electrospinning. As the solvent rapidly evaporated and PVA fibers solidified, the SiO_2 nanoparticles became embedded within or attached to the fiber surface. Due to the high surface energy and charge density of SiO_2, some nanoparticles locally clustered, forming small SiO_2-rich domains that appeared as bead-like protrusions in the SEM images. With increasing SiO_2 content, these aggregates became more pronounced (Supplementary Fig. S5), exhibiting sizes of ~0.5–5 μm, much larger than the individual SiO_2 nanoparticles (20–30 nm). Such micron-scale domains are comparable to the wavelength range of solar radiation (0.3–2.5 μm), thereby maximizing scattering efficiency. Consequently, the hierarchical multiscale structure—comprising the nanofiber network, micro-scale pores, and SiO_2-rich domains—facilitates multi-directional light scattering and significantly enhances diffuse reflectance, leading to the high solar reflectance and strong AW (8–13 μm) emissivity observed in Fig. 2a.

Contact angle analysis revealed a dose-dependent increase in hydrophobicity. Pristine PVA and PVA/SiO_2 showed very low contact angles of 5.9° and 8.0°, respectively (Fig. 3f). Upon EO incorporation, contact angles increased to 119.0° at 0.25 wt% and 125.6° at 0.5 wt%. Notably, RCD with 0.5 wt% EO maintained its water-repellent surface for over 5 min without moisture penetration (Supplementary Fig. S6), underscoring its capacity to preserve structural integrity in sweating or humid environments.

Water vapor permeability of the RCD was quantitatively assessed by water vapor transmission rate (WVTR) testing (Supplementary Fig. S7). The RCD had a WVTR of 198 ± 8 g m^{-2} h^{-1}, surpassing both clinically representative four-ply gauze (183 ± 17) and CAB (19 ± 7) (Fig. 3g). This increased permeability is primarily attributable to the electrospun nanofibrous architecture of the RCD, which forms a highly porous and interconnected network that facilitates efficient moisture diffusion. Importantly, although hydrophobically modified through EO incorporation, the RCD maintained its vapor-permeable nanoporosity, thereby repelling liquid water while still permitting water vapor transport. This dual functionality of water resistance and vapor permeability ensures moisture regulation, preventing exudate accumulation and minimizing the risk of maceration while preserving structural integrity in humid environments.

Swelling tests (Fig. 3h) further confirmed the RCD's high exudate uptake capacity, with a swelling ratio of 137 ± 5%, markedly surpassing gauze (39 ± 4%) and CAB (5 ± 2%). This large uptake capacity is beneficial for wound management, as it helps absorb excessive exudates, maintain a moist healing environment, thereby supporting tissue regeneration. These features underscore the RCD's suitability as effective wound dressing.

To further evaluate the biological properties of the RCD, we measured antibacterial activity, drug release behavior, intracellular antioxidative performance and cytocompatibility by integrating C-PC. RCD antibacterial activity was evaluated against two common bacteria in skin wounds[66,67]. Gram-positive Staphylococcus aureus (*S. aureus*) and gram-negative Escherichia coli (*E. coli*)

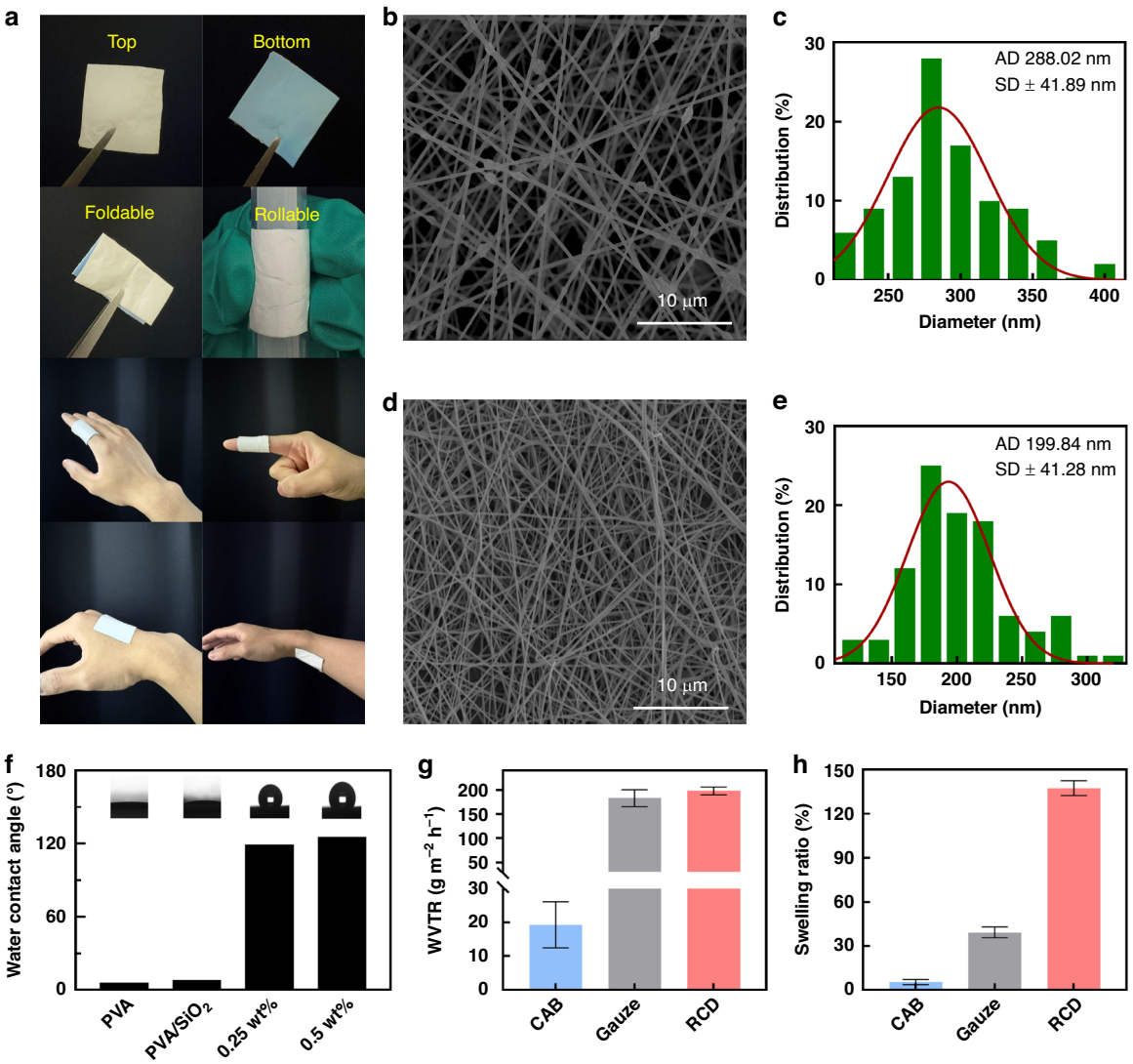

Fig. 3 Physicochemical and morphological characterization of the RCD. a Photographs of the bilayer configuration showing the top RC layer (white) and bottom drug-loaded layer (blue), together with mechanical flexibility (foldable, rollable) and self-adhesion to moist human skin enabled by the hydrophilic bottom layer. **b**, **c** Scanning electron micrograph and corresponding fiber diameter distribution of the RC layer with randomly embedded SiO_2 nanoparticles (1.96 wt%). **d**, **e** Scanning electron micrograph and fiber diameter distribution of the drug-loaded layer. **f** Static water contact angle of PVA and PVA/SiO_2 composites with varying eugenol (EO) content (0–0.5 wt%). **g** Water vapor transmission rate (WVTR) of commercial adhesive bandage (CAB), gauze, and RCD. **h** Swelling ratios of CAB, gauze, and RCD

(Fig. 4a, b). Increasing the C-PC content within the RCD led to a progressive enlargement of the inhibition zones, with the highest concentration (20 wt%) yielding diameters of 26 mm for *S. aureus* and 11 mm for *E. coli* (Supplementary Table S1). In contrast, the pristine PVA sample without C-PC exhibited no inhibition beyond the disc diameter (6 mm). These results demonstrate that C-PC incorporation imparts strong, dose-dependent antibacterial efficacy across diverse bacterial species, enabling RCD to actively inhibit bacterial colonization, which is a critical requirement for infection control in wound care.

To measure the release kinetics of C-PC, RCD samples were immersed in phosphate-buffered saline (PBS) at 37 °C, and cumulative release was quantified over 96 h using spectrophotometry (Fig. 4c). All samples exhibited a biphasic release profile with an initial burst followed by a slower, sustained release. This behavior reflects the hierarchical distribution of C-PC within the nanofibrous matrix, from which surface-associated molecules were rapidly released, whereas those embedded deeper within the polymer network diffused through the dense fiber core over time. The cumulative release increased with C-PC loading, reaching 35 ± 4%, 43 ± 3%, and 51 ± 3% for

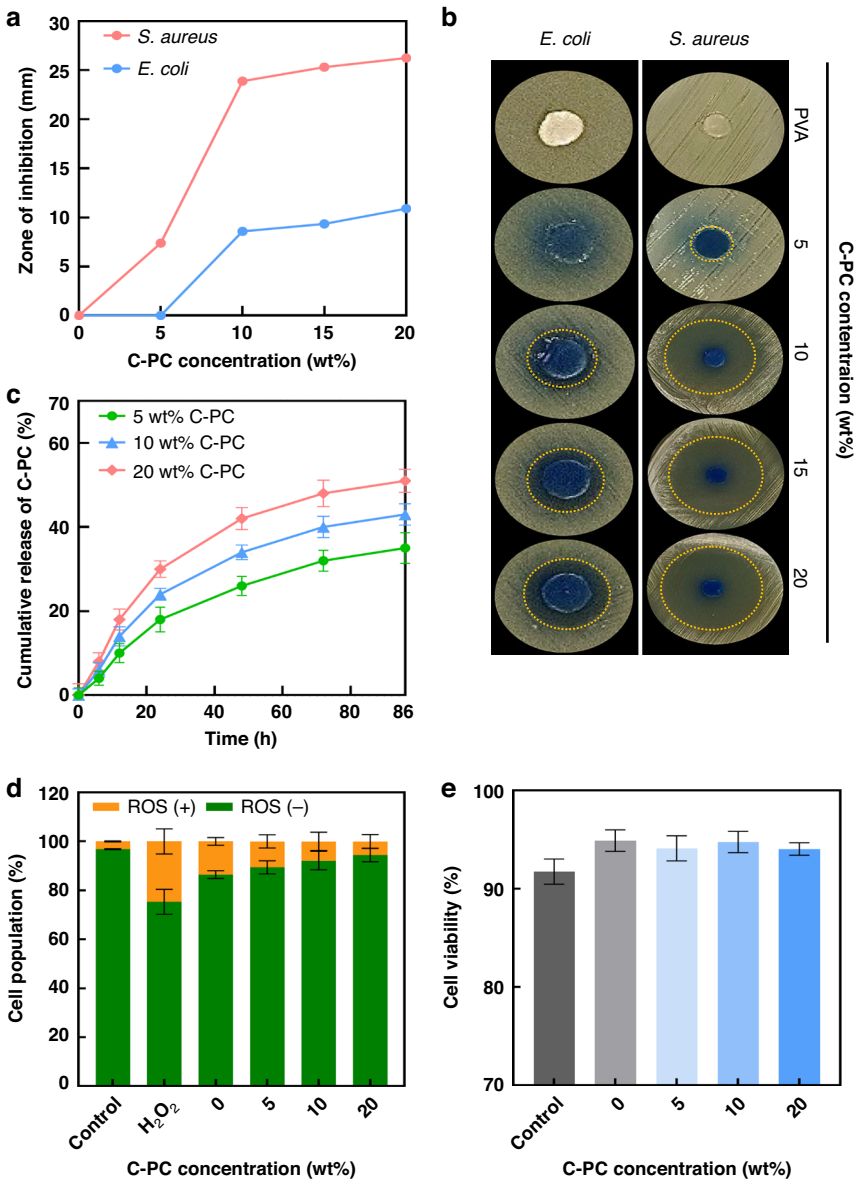

Fig. 4 Antibacterial, antioxidative, cytocompatibility, and C-PC release profiles. a Quantification of inhibition zone diameters. **b** Representative images showing inhibition of growth of *S. aureus* (right) and *E. coli* (left) as a function of RCD C-PC content. **c** Cumulative release profile of C-PC from RCD as a function of C-PC content and time. **d** Ratio of ROS-negative to ROS-positive L-929 cells under oxidative stress (H_2O_2). **e** Cell viability of L-929 fibroblasts, demonstrating the cytocompatibility of RCD with varying C-PC concentrations

the 5, 10, and 20 wt% samples, respectively. Importantly, sustained release was achieved in PBS, which closely mimics the ionic strength and composition of wound exudates, underscoring the relevance of these findings for in vivo applications. Because the RCDs were fully immersed during testing, they remained in a saturated swelling state, representing the upper bound of diffusion behavior expected under real moist wound conditions. Therefore, variations in ambient humidity are expected to have only a negligible effect on the overall release kinetics. This ability of the RCDs to sustain release without premature depletion further highlights their clinical promise for controlled bioactive delivery in dynamic wound environments.

To probe antioxidant performance, intracellular ROS levels were quantified in L929 fibroblasts exposed to H_2O_2 (Fig. 4d). H_2O_2 exposure alone increased the ROS-positive cell population to 25 ± 5%, indicating substantial oxidative stress, while reducing the ROS-negative population to 75 ± 5%. Treatment with RCD containing C-PC significantly reduced the ROS-positive fraction in a concentration-dependent manner, reaching 5.6 ± 2.8% at

20 wt% C-PC. Correspondingly, ROS-negative cells increased to 94 ± 3%, a 77% reduction in oxidative damage relative to the stressed group. This pronounced intracellular scavenging highlighted the ability of RCD to restore redox homeostasis at the cellular level, which is a key function in suppressing inflammation, protecting regenerating tissue, and facilitating healing under oxidative stress. Unlike conventional antioxidant assays, such as DPPH, which rely on extracellular chemical reactions, this result provides direct evidence of in situ antioxidant functionality within live cells.

Cytocompatibility was evaluated following 24 h exposure of L929 fibroblasts to RCDs with varying C-PC concentrations (Fig. 4e). Viability remained consistently high across all samples, with 20 wt% C-PC exhibiting 94 ± 1% viability. This confirms that biofunctionalized RCD does not elicit cytotoxic effects even under extended direct contact conditions, thereby satisfying the clinical safety standards for wound contact materials. These findings demonstrated that RCD meets the key biological benchmarks for advanced wound care, offering effective antibacterial action, intracellular ROS suppression, sustained release of C-PC, and high cytocompatibility to support a regenerative wound environment.

To evaluate the real-world cooling performance of the RCD under direct sunlight, we developed a thermally isolated temperature-monitoring chamber on an outdoor rooftop (Fig. 5a). To replicate physiologically relevant conditions, simulated skin was employed to mimic human skin thermal behavior and assess the localized cooling efficacy of the RCD. The simulated skin included a polyimide-insulated flexible heater operating at a constant input power of 104 Wm^2, maintaining a physiological range of 32–35 °C (Supplementary Fig. S8). Four types of dressings (bare (no dressing), CAB, gauze, and RCD) were applied (Fig. 5b). The experiment was conducted from 11:30 to 14:00 (2025.07.10), with direct solar exposure initiated at 12:00. Prior to sunlight exposure, all simulated skin samples had baseline temperatures of 30–32 °C, as verified by thermal infrared camera (Fig. 5d). Upon exposure to intense sunlight (relative humidity (RH) = 16.7%, wind speed (WS) = 0.087 m s^{-1}; Supplementary Fig. S9a). RCD maintained a mean temperature of 34.9 °C with a maximum of 36.4 °C, well within normal skin temperature range. In contrast, the bare, CAB, and gauze samples reached mean temperatures of 54.5, 52.5, and 49.6 °C, with peak values of 61.8, 57.2, and 53.0 °C, which are known to induce thermal stress and potential tissue damage.

The outstanding temperature reduction exhibited by the RCD can be ascribed to its optimized optical properties, characterized by a high solar reflectance of 0.92 and emissivity of 0.92 within the AW (Supplementary Fig. S4). By comparison, while CAB and gauze possess high AW emissivity (0.91 and 0.83, respectively), their relatively low solar reflectance (0.39 for CAB and 0.44 for gauze) limit their ability to mitigate solar heat gain (Supplementary Fig. S10). Gauze was applied in four layers (total thickness 0.48 mm), mimicking the typical clinical configuration, whereas CAB was tested as a single layer (thickness 0.9 mm). Despite its substantially thinner structure (0.3 mm), RCD exhibited a better cooling performance (Fig. 5e). Although greater thickness increases thermal resistance, RCD's optical properties enable suppression of solar heat gain while facilitating heat dissipation (Supplementary Table S2).

To separate the intrinsic RC effect of the RCD from convective influences, we next enclosed the samples in a polyethylene (PE) film during outdoor measurements (Fig. 5c). Under these conditions (2025.07.11, RH = 21.5%, WS = 0.234 m s^{-1}; Supplementary Fig. S9b), RCD maintained an average temperature of 36.2 °C, while the ambient temperature reached 49.6 °C, yielding a temperature reduction of 13.5 °C. Even in the absence of PE film, RCD exhibited a consistent average cooling effect of 8 °C below ambient (Supplementary Fig. S11). These results demonstrate that the RCD effectively maintains skin surface temperatures within the physiological range (<37 °C, consistent with the upper limit of normal skin temperature), remaining well below ambient levels under intense sunlight owing to its optimized optical properties.

To more rigorously assess RCD functionality, we established a full-thickness murine excisional wound model in mice, enabling direct evaluation of its therapeutic efficacy arising from both thermal regulation and sustained C-PC release (Fig. 6). This system was designed to simultaneously assess localized thermal modulation and wound-healing efficacy under conditions that reliably elevated wound surface temperatures to levels equivalent to those produced by direct outdoor sunlight, thereby serving as a physiologically relevant surrogate for solar heat stress. Rather than relying on outdoor exposure, a daylight lamp can induce heat stress, closely resembling that experienced under direct solar exposure (Fig. 6a). This approach minimizes environmental variability and mitigates risks, such as infection, insect interference, and animal stress, while enabling reproducible and clinically relevant heat loading. The distance between the lamp and mouse was pre-validated to mimic heat stress typically encountered during direct outdoor solar exposure (Supplementary Fig. S12).

Six-mm circular excisional wounds were created on the dorsal skin of BALB/c mice with a thermocouple probe affixed onto the wound bed to enable continuous temperature monitoring[68] (Fig. 6a). Mice were randomly assigned to one of three treatment conditions: bare (no dressing), CAB, or RCD (Supplementary Fig. S13). During 30 min of lamp exposure, animals were gently

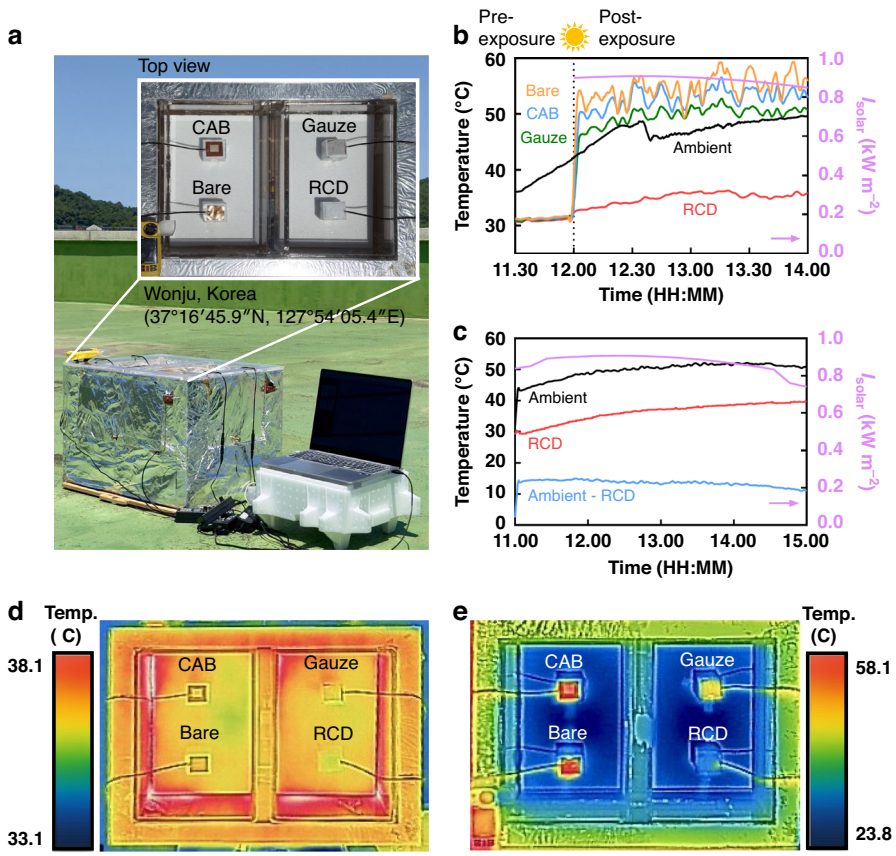

Fig. 5 Outdoor cooling performance using simulated skin. a Photographs of the rooftop testing setup (37°16′45.9″N, 127°54′05.4″E). The inset shows a top-down view of the enclosed chamber housing four simulated skin modules, each covered with a different dressing, alongside an environmental monitoring system. **b** Time-dependent surface temperatures of simulated skin under natural convection during solar exposure, along with corresponding solar irradiance (I_{solar}) profiles. **c** Surface temperatures of RCD and ambient measured under direct sunlight with convective heat transfer suppressed using a polyethylene film enclosure, isolating intrinsic RC performance. Solar irradiance (I_{solar}) profiles are shown simultaneously. Infrared thermal images before (**d**) and after (**e**) solar exposure in the experiment shown in (**b**)

immobilized using soft fabric restraints, and wound surface temperatures were continuously recorded (Supplementary Fig. S14).

RCD-treated wounds-maintained temperatures below 37 °C throughout light exposure, with a peak temperature of 36.3 °C (Fig. 6b). In contrast, wounds treated with CAB and bare exceeded the physiological threshold of 37 °C, reaching peak temperatures of 40.2 °C and 42.9 °C, respectively. Notably, this thermal response under lamp irradiation closely mirrored the rooftop findings for the simulated skin (Fig. 5b), where bare and CAB exceeded 40 °C under direct sunlight, while RCD kept simulated skin below 37 °C. The concordance between outdoor and lamp-based results confirmed that lamp irradiation reliably reproduced the heat stress of natural sunlight, validating it as a physiologically relevant surrogate. This further verified that the cooling benefit of RCD observed in simulated skin was consistently reproduced in murine wounds. The cooling effect observed in RCD-treated dorsal wounds is solely attributable to its RC properties, as murine dorsal skin lacks eccrine sweat glands and therefore cannot perform autonomous thermoregulation[69]. These in vivo findings highlight the capacity of the RCD to passively shield wounds from external heat while sustaining conditions favorable for healing.

To assess therapeutic outcomes, wound contraction was evaluated over seven days in four groups ($n = 12$ per group): bare, CAB, RCDM (RCD without the drug-loaded layer), and RCD (Fig. 6c, see Supplementary Figs. S15–S19 for settings). An RC layer-only (RCDM) group was included to isolate the effect of RC alone, allowing direct comparison with the full RCD to clarify the additional benefits provided by C-PC release. Starting one day after wound creation and dressing application, mice were exposed to lamp for 1 h daily for six consecutive days (Supplementary Fig. S16). This exposure time lies within the physiologically relevant range of solar heat stress typically encountered during practical outdoor activities,

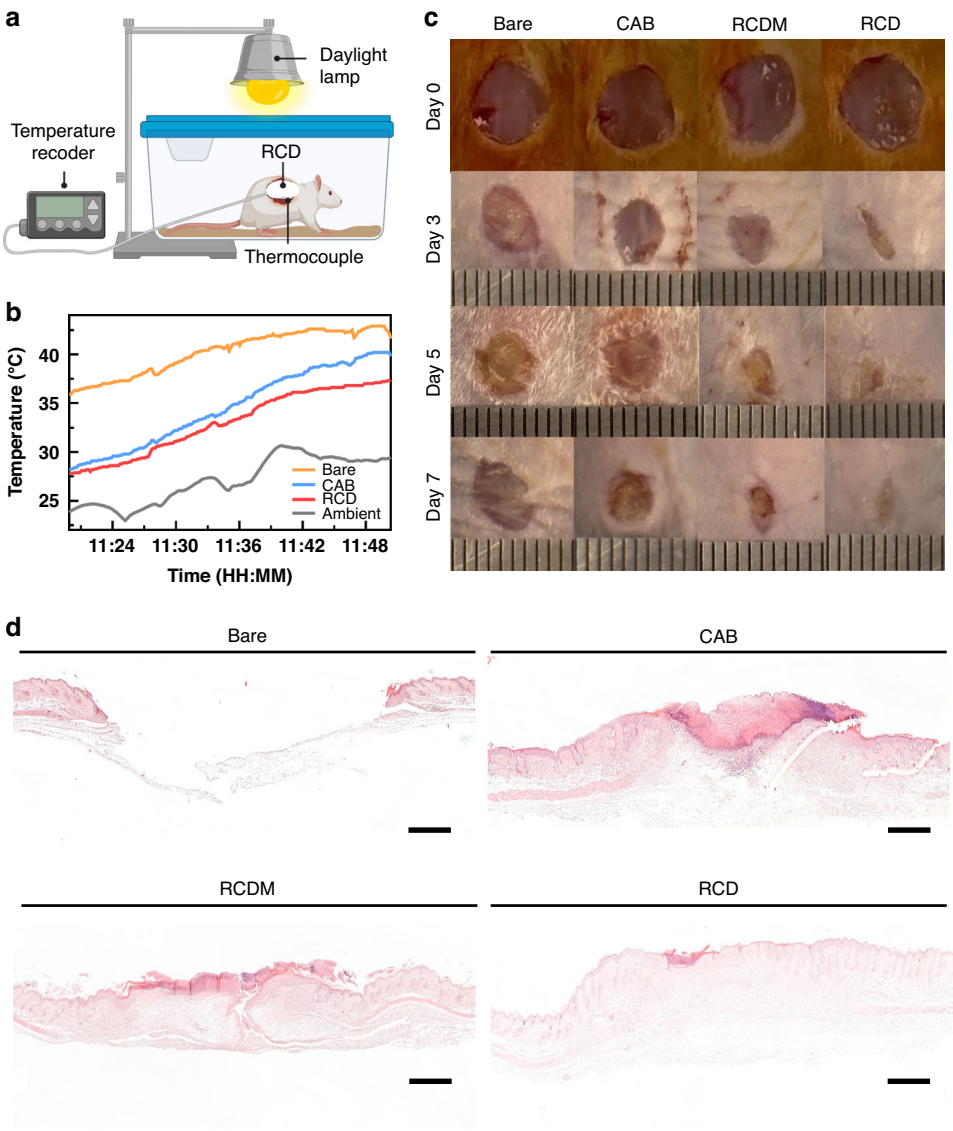

Fig. 6 In vivo wound healing and temperature monitoring. a Experimental setup schematic. A thermocouple was affixed directly to the wound, followed by dressing and fixation with transparent film. **b** Wound surface temperature profiles recorded during lamp exposure. **c** Representative images of wounds on days 0, 3, 5, and 7 post-treatment ($n = 12$ mice per group; total $n = 48$). **d** Hematoxylin and Eosin (H&E)-stained sections of wounds collected on day 7 post-treatment, illustrating differences in re-epithelialization and dermal remodeling. (4× magnification; scale bar, 1 mm). **a** Created with BioRender.com

with skin temperatures known to rise significantly within the first hour of direct sun exposure[70,71]. The lamp reproduced a controlled thermal environment comparable to heat stress under direct outdoor sunlight (Supplementary Fig. S17). Wound areas were quantified on days 3, 5, and 7 using digital calipers (Supplementary Fig. S18). This experimental design enabled the direct evaluation of both the cooling performance and therapeutic efficacy of sustained C-PC release.

Wound contraction analysis revealed that the RCD group consistently outperformed all the other groups across the entire observation period (Fig. 6c). By day 7, wounds treated with RCD exhibited near-complete closure (90.25 ± 2.38%), substantially higher than those treated with RCDM (71.55 ± 3.12%), CAB (47.97 ± 3.45%) and bare (42.80 ± 4.92%) (Supplementary Fig. S20). In the early phase of the experiment, a similar trend was observed, with the RCD group demonstrating superior closure on day 3 and maintaining its lead until day 5. Quantitatively, this represents a 1.88-fold improvement over CAB and a 2.11-fold enhancement relative to the bare group. Compared to RCDM, which benefits from

thermal modulation alone, RCD achieved a 1.26-fold greater contraction rate, highlighting the additive therapeutic value of sustained C-PC release. These findings demonstrate that the integrated combination of thermal protection and bioactive drug delivery underlies the superior wound-healing outcomes of RCD.

To investigate the mechanisms underlying the wound regeneration induced by RCD treatment, we analyzed skin tissues harvested on days 3, 5, and 7 post-treatment (Fig. 6d, Supplementary Figs. S21–S26). On day 3 (Supplementary Figs. S21, S23), bare and CAB wounds remained in the inflammatory phase with fibrin deposition and incomplete epithelium, closely resembling freshly wounded tissue (positive control) (Supplementary Fig. S26). RCDM wounds showed partial inflammatory resolution with modest collagen, while RCD wounds had already entered the proliferative phase with epithelial migration and early collagen formation. By day 5 (Supplementary Figs. S22, S24), bare and CAB wounds still showed incomplete epithelial coverage and disorganized tissue. RCDM wounds formed a continuous but immature epidermis, whereas RCD wounds achieved full re-epithelialization with stratified epidermis, reduced inflammation, and organized collagen bundles with early neovascularization. Detailed histological descriptions of day 3 and day 5 wound tissues are provided in Supplementary Note S2.

On day 7, RCD-treated wounds exhibited near-complete morphological restoration (Fig. 6d, Supplementary Fig. S25). In contrast, the bare and CAB wounds remained in a state of incomplete repair with epithelial discontinuities, unresolved inflammatory foci, and irregular collagen deposition. RCDM-treated wounds approached closure but lacked full epidermal stratification and matrix organization, and exhibited a relatively thickened epidermis, likely indicative of reactive hyperplasia and incomplete remodeling. Strikingly, RCD-treated wounds displayed a fully regenerated, well-stratified epidermis with physiological thickness, an intact basement membrane, and minimal immune-cell infiltration. Masson's Trichrome (MT) staining revealed compact reticular collagen bundles arranged in a lamellar configuration, closely resembling the dermal matrix of healthy, unwounded skin. These observations were corroborated by the histological analysis of normal skin (negative control) (Supplementary Fig. S26), confirming that RCD treatment restored both epidermal architecture and dermal organization to a state nearly indistinguishable from baseline.

These results demonstrate that RC is critical for mitigating heat-induced tissue damage, whereas sustained C-PC delivery contributes to accelerated inflammation resolution, oxidative stress modulation, and organized tissue remodeling. RCD expedites wound closure and promotes a healing trajectory that more closely resembles physiological skin regeneration. This dual-function approach provides an effective means of maintaining a regenerative microenvironment under thermally adverse conditions and highlights the potential of RCDs as advanced wound dressings for use in challenging outdoor environments.

Discussion

In summary, this study demonstrates that a radiative cooling dressing integrating passive cooling with sustained C-phycocyanin delivery accelerates wound healing under heat stress. The dressing exhibited 92% of solar reflectance and mid-infrared emissivity, and simulations further demonstrated its effective performance across diverse climatic conditions. The high reflectance minimizes solar absorption, whereas the strong mid-infrared emissivity facilitates radiative heat dissipation to the atmosphere, enabling efficient passive cooling. The dressing also met key requirements of a wound dressing. It repelled sweat and external moisture and permitted vapor transmission to prevent excessive humidity. Moreover, it swelled to absorb exudates and naturally adhered to the wound surface, while maintaining sufficient flexibility for conformal coverage. Even under fully swollen conditions, the RCDs exhibited gradual and controlled release, suggesting that in real wound environments, C-phycocyanin would be continuously delivered to the tissue, thereby enabling sustained suppression of oxidative stress and prevention of bacterial infection at the wound site while maintaining cytocompatibility. Under outdoor sunlight, the radiative cooling dressing reduced surface temperatures by up to 15.2 °C below ambient and consistently maintained simulated skin within physiological limits (<37 °C), averaging 16.1 °C cooler than commercial dressings that consistently exceeded 40 °C. In vivo, similar thermal reduction was confirmed under solar-simulated heat stress, only the radiative cooling dressing maintained wound bed temperatures below 37 °C and accelerated closure to 90 ± 2% by day 7—nearly twice as fast as commercial dressings. The accelerated healing process was accompanied by complete epithelial regeneration and organized collagen remodeling. Although the in vivo experiments were conducted under a lamp-based solar simulation rather than direct sunlight, the results from the simulated skin setup under real outdoor conditions support the effective performance of the RCD in mitigating thermal stress, demonstrating better temperature reduction than commercial dressings with similar mid-infrared emissivity.

These findings highlight the advantage of integrating radiative cooling with therapeutic drug delivery within a single wound dressing. By directly distinguishing the effects of passive cooling from those of C-phycocyanin

release, our study shows that their combination is important to achieve enhanced healing outcomes under heat stress. Unlike previous studies that focused on either thermal management or drug delivery alone, this work demonstrates the combined contribution of radiative cooling and bioactive effects to enhanced wound healing under heat stress. This work not only presents a practical dressing that performs consistently in both in vitro and in vivo settings but also establishes a broader strategy for designing multifunctional materials that couple passive thermal management with therapeutic delivery. Such an approach offers a promising strategy to effective wound care in thermally stressed outdoor environments and may inspire wider applications of radiative cooling technology in biomedical treatment.

Materials and methods

Fabrication

To prepare the drug-loaded layer, 0.4 g of C-PC (Sigma-Aldrich, USA) was dispersed in 20 mL of 10 wt% PVA (89% alcoholysis; Avention, Korea) solution, followed by ultrasonication and magnetic stirring. For the RC layer, 7 g of EO (Avention, Korea) and 2 mL of Tween-80 (Avention, Korea) were mixed into 100 mL of 10 wt% PVA (99% alcoholysis; Avention, Korea). Then 1.96 wt% of SiO_2 nanoparticles (Avention, Korea) were added, and the mixture was sonicated and stirred. The bilayer RCD was fabricated through sequential electrospinning: 4 mL of PVA/C-PC solution was electrospun at 20 kV, followed by 5 mL of EO/PVA/SiO_2 solution electrospun at 18.5 kV onto the underlying layer.

Spectral characterization and simulation

Reflectivity and emissivity were measured using a UV–VIS–NIR spectrophotometer (V-770, Jasco, Japan) in the 0.3–2.5 μm range and a Fourier transform infrared (FT-IR) spectrometer (Vertex 70 v, Bruker, Germany) in the 2.5–18 μm range. Electrospun films were analyzed as self-standing samples, and an integrating sphere was employed to collect both specular and diffuse reflected light from the fibrous porous surface. Spectral emissivity $\varepsilon(\lambda)$ was calculated using the relation $\varepsilon(\lambda) = 1 - R(\lambda) - T(\lambda)$, assuming negligible internal absorption within each polymer layer. To further assess the practical radiative cooling performance, spectral data were input into ViBA Rad, a dedicated simulation tool for evaluating the performance of radiative cooling materials under various environmental conditions. For Fig. 2a, measurements were performed on the RC layer only (EO/PVA and EO/PVA/SiO_2) across varying SiO_2 loadings; Supplementary Fig. S3 reports drug-loaded layer only (C-PC/PVA) emissivity within the 8–13 μm AW; and Supplementary Fig. S4 presents full-stack reflectance and emissivity of the complete bilayer RCD combining the optimized RC layer with 1.96 wt% SiO_2 and the drug-loaded layer.

Physicochemical characterization

Water contact angle

Angles were measured using a goniometer (DSA100, KRÜSS GmbH, Germany) after placing 5 μL of deionized water on each film surface. For PVA and PVA/SiO_2 samples, images were captured every 10 ms over 5 s. For EO/PVA/SiO_2 samples containing 0.25 wt% and 0.5 wt% EO, images were taken every 5 s over 5 min. All samples were individually measured under ambient conditions.

Water vapor transmission

RCD permeability of RCD samples was measured using a modified water-filled beaker method. Circular dressing films were sealed over the mouths of glass beakers (50-mm diameter) filled with 50 mL deionized (DI) water. Beakers were placed on a hot plate and maintained at 40 °C to generate a continuous water vapor flux, then exposed to ambient laboratory conditions (25 ± °C, 50 ± 5% RH) for 6 h. The change in mass caused by evaporation was recorded using a precision balance; Water vapor transmission ratios were calculated using the equation:

$$WVTR = \frac{\Delta m}{A \times t}$$

where m is weight loss (g), A is exposed surface area of the dressing (m^2), and t is the test duration. Data are presented as means ± standard deviation (SD).

Swelling

RCD samples were immersed in DI water at 37 °C for 2 h. After incubation, surface water was gently blotted off, and weights were recorded. The swelling ratio (%) was calculated as:

$$Swelling\ ratio(\%) = [(W_t - W_0/W_0)] \times 100$$

where W_o and W_t are the initial dry weight and the swollen weight after immersion, respectively. Data are presented as means ± standard deviation (SD).

Electrospun fiber morphology

Scanning electron microscopy (SEM) was used to investigate the surface morphology and microstructure of the electrospun fibers. The fiber diameter distributions were quantitatively analyzed from the SEM images using the ImageJ software (version 1.53t, National Institutes of Health, USA)[72], based on measurements of over 100 randomly selected fibers.

Antibacterial activity

Standard disc diffusion was used to measure activity against *Staphylococcus aureus* (KTCC 1916) and

Escherichia coli (KTCC 2441). RCD samples (6-mm diameter) containing C-PC (0, 5, 10, 15, and 20 wt.%) were placed onto Mueller-Hinton agar plates that had been uniformly seeded with bacterial suspensions at ~1 × 10 CFU/mL. After incubation at 37 °C for 24 h, the diameters of the inhibition zones around each sample were measured using ImageJ software to quantify antibacterial activity.

Antioxidative activity

Intracellular reactive oxygen species (ROS) levels were quantified using the Muse® Oxidative Stress Kit (MCH100111, Luminex Corporation, Austin, TX, USA). The murine cell line NCTC clone 929 (L-929; KCLB No. 10001) obtained from the Korean Cell Line Bank (KCLB, Seoul, Korea) was pre-treated with H_2O_2 to induce oxidative stress, then exposed to membranes containing C-PC at 0, 5, 10, or 20 wt% for 24 h. Cells were harvested, washed with PBS, and resuspended in 1× Assay Buffer. For each sample, 10 µL of cell suspension was mixed with 190 µL of ROS reagent working solution, incubated at 37 °C for 30 min in the dark, and analyzed using the Muse® Cell Analyzer (Luminex). Data is presented as means ± standard deviation (SD).

Cytocompatibility

RCD cytocompatibility was assessed using L-929 cells and the Muse® Count & Viability Kit (MCH100102, Luminex). Cells were seeded at a density of 1×10^6 per well and incubated in RPMI 1640 medium supplemented with 10% FBS and 1% penicillin-streptomycin at 37 °C under 5% CO_2. After 24 h of stabilization, cells were treated with RCD containing C-PC at concentrations of 0, 5, 10, or 20 wt%, incubated for another 24 h, harvested using trypsin-EDTA, pelleted at 1000 rpm for 5 min, and resuspended in PBS. Subsequently, 50 µL of cell suspension was mixed with 50 µL of viability reagent from the Muse® kit, incubated for 5 min at room temperature in the dark, and analyzed using the Muse® Cell Analyzer (Luminex). Data is presented as means ± standard deviation (SD).

C-PC release

Electrospun nanofiber mat samples containing 5, 10, or 20 wt% C-PC were prepared and cut into 2 × 2-cm squares. Prior to the assay, all samples were weighed and trimmed to ensure that each had a mass of 50 ± 1 mg to reduce variation in initial drug loading. Each sample was immersed in 10 mL of phosphate-buffered saline (PBS; pH 7.4) and incubated at 37 °C with gentle shaking (50 rpm) to simulate physiological conditions. At 1, 3, 6, 12, 24, 48, 72, and 96 h, 1-mL aliquots of the release medium were withdrawn and replaced with an equal volume of fresh PBS to maintain sink conditions and constant volume. The concentration of the released C-PC in the collected medium was measured using UV–VIS spectrophotometry at 620 nm, the maximum absorbance wavelength of C-PC. Absorbance values were converted to concentrations using a standard calibration curve. Cumulative release was calculated using the equation:

$$Cumulative\ release(\%) = \left(\frac{M_t}{M_\infty}\right) \times 100$$

where M_t is the total amount of C-PC released into the medium up to time t and M_∞ represents the total loaded amount of C-PC in each sample, determined by complete dissolution of parallel samples. All measurements were performed in triplicate, and data are presented as means ± standard deviation (SD).

Outdoor thermal evaluation

RCD cooling performance was assessed in outdoor conditions. The setup consisted of a wooden chamber fully wrapped in aluminum foil to minimize external thermal interference, with an acrylic enclosure to further suppress conductive heat transfer. To reduce contact with the ground, the chamber was elevated approximately 1 m above the surface, thereby minimizing conductive heat exchange with the substrate. All measurements were conducted on the rooftop of Yonsei University (Wonju, South Korea) under clear skies. For static material surface measurements, samples were placed atop a Styrofoam block within the acrylic enclosure, and thermocouples were affixed to the bottom surface. Data acquisition was performed using a multichannel data-logging thermometer (HH520; Omega Engineering). Measurements were conducted on July 7, 2025 (Supplementary Fig. S1c). For evaluation on skin-mimicking substrates (Fig. 5b), conducted on July 10, 2025, a skin simulation was employed, comprised of a polyimide-insulated flexible heater operated at a constant power density of 104 W m^{-2}. RCD, gauze, and CAB were directly applied to the heater surface, and temperatures were recorded using thermocouples placed beneath each film. Subsequent tests (Fig. 5c) were performed on July 11, 2025. Concurrent environmental parameters, including UV intensity, RH, and WS, were continuously monitored using an HWS1000 weather station (Zoglab Microsystem). Solar irradiance data were obtained from the Korean Meteorological Administration. Infrared thermographic imaging was performed using a handheld thermal camera (E6390, Teledyne FLIR Systems).

Murine wound model

All animal experiments were performed in compliance with institutional guidelines and approved by the Institutional Animal Care and Use Committee (IACUC) of

Yonsei University MIRAE Campus, in accordance with the regulations of the Association for the Assessment and Accreditation of Laboratory Animal Care International (approval no. YWCI-202504-008-01).

Forty-eight female BALB/c mice (8 weeks old; Jun Biotech, Korea) were anesthetized by inhalation of isoflurane using a nose cone. Dorsal hair was removed using electric clippers, followed by depilatory cream. Exposed skin was disinfected with povidone-iodine. Dorsal full-thickness excisional wounds (6-mm diameter) were created using a sterile biopsy punch. Mice were randomly assigned to four groups ($n = 12$ each): (1) untreated wounds (Bare), (2) covered with CAB, (3) treated with the RC layer only, without the drug-loaded layer (RCDM), and (4) treated with the complete bilayer RCD with both RC and drug-loaded layers (RCD). To prevent dressing displacement, a transparent medical film was applied to all wound sites, including those in the bare group. Healing was assessed over a 7-day period, and animals were euthanized by CO_2 inhalation in a chamber on days 3, 5, and 7 ($n = 4$ per group at each time point). At each of these points, wound areas were measured using a digital caliper. No experimental units or data points were excluded from the analysis, and all mice remained healthy throughout the study. Wound contraction rates were determined using the formula:

$$Wound\ contraction(\%) = \left(\frac{A_0 - A_t}{A_0}\right) \times 100$$

where A_0 is the initial wound area (day 0) and A_t is the remaining wound area at time t. Data is presented as means ± standard deviation (SD). Wound tissues were excised, fixed in 4% paraformaldehyde, embedded in paraffin, sectioned, and stained using hematoxylin and eosin (H&E) and MT.

Histological analysis of wound healing progression

Wound tissues were excised from mice on days 3, 5, and 7 after treatment and fixed in 4% paraformaldehyde at 4 °C for 24 h. The fixed samples were dehydrated using a graded ethanol series, embedded in paraffin, and sectioned at a thickness of 4 µm using a rotary microtome. The tissue sections were stained with H&E and MT, protocols according to standard histological procedures.

Statistical analysis

All quantitative data are presented as mean ± standard deviation (SD). Wound closure and histological results were evaluated under blinded conditions to ensure transparency and reproducibility.

Ethics declarations

All animal procedures were approved by the Institutional Animal Care and Use Committee (IACUC) of Yonsei University MIRAE Campus (approval YWCI-202504-008-01).

Acknowledgements

D.L. acknowledges the National Research Foundation (NRF) grant (RS-2025-00556856) funded by the Ministry of Science and ICT (MSIT) of the Korean government. M.K. acknowledges the NRF grant (RS-2025-23524064) funded by the MSIT of the Korean government.

Author details

[1]Department of Biomedical Engineering, Yonsei University, Wonju 26493, Republic of Korea. [2]Department of Biomedical Laboratory Science, Graduate School, Eulji University, Uijeongbu 11759, Republic of Korea. [3]Department of Biomedical Laboratory Science, College of Software Digital Healthcare Convergence, Yonsei University, Wonju 26493, Republic of Korea. [4]Department of Mechanical and Robotics Engineering, Gwangju Institute of Science and Technology (GIST), Gwangju 61005, Republic of Korea

Author contributions

C.H. conceived and designed the study, prepared the materials, and performed experiments encompassing characterization, biological assessments, outdoor thermal measurements, and in vivo wound healing. He analyzed the data, generated the figures and schematics, and drafted and revised the manuscript. H.L. performed biological experiments and contributed to data analysis. W.-S.K., S.-M.K., and K.-J.K. conducted in vivo wound-healing experiments, performed histology, and assisted with data interpretation. J.B. performed FT-IR spectroscopy and SEM imaging. M.K. provided manuscript editing, resources, and funding. K.J.R. supervised animal experiments and provided resources. S.H. supervised biological experiments and provided resources. D.L., the principal investigator supervised the project, contributed to conceptual development, advised on experimental design and data interpretation, and provided guidance, manuscript editing, project coordination, and secured funding.

Competing interests

The authors declare no competing interests.

Supplementary information The online version contains supplementary material available at https://doi.org/10.1038/s41378-026-01188-2.

Received: 10 October 2025 Revised: 19 November 2025 Accepted: 8 December 2025
Published online: 13 April 2026

References

1. Lee, H. J. & Kim, M. Skin barrier function and the microbiome. *Int. J. Mol. Sci.* **23**, https://doi.org/10.3390/ijms232113071 (2022).
2. Yang, Y., Qu, L., Mijakovic, I. & Wei, Y. Advances in the human skin microbiota and its roles in cutaneous diseases. *Microbial. Cell Factories* **21**, 176 (2022).
3. Trompette, A. & Ubags, N. D. Skin barrier immunology from early life to adulthood. *Mucosal Immunol.* **16**, 194–207 (2023).
4. Yousef, H., Alhajj, M. & Sharma, S. *Anatomy, Skin (Integument), Epidermis* (StatPearls Publishing, 2020).
5. Tottoli, E. M. et al. Skin wound healing process and new emerging technologies for skin wound care and regeneration. *Pharmaceutics* **12**, 735 (2020).
6. Zhou, S. et al. New insights into balancing wound healing and scarless skin repair. *J. Tissue Eng.* **14**, https://doi.org/10.1177/20417314231185848 (2023).
7. Shpichka, A. et al. Skin tissue regeneration for burn injury. *Stem Cell Res. Therapy* **10**, 94 (2019).
8. Witte, M. B. & Barbul, A. General principles of wound healing. *Surg. Clin. North Am.* **77**, 509–528 (1997).
9. Landén, N. X., Li, D. & Ståhle, M. Transition from inflammation to proliferation: a critical step during wound healing. *Cell. Mol. Life Sci.* 73, 3861–3885 (2016).

10. Gonzalez, A. C. O., Costa, T. F., Andrade, Z. A. & Medrado, A. R. A. P. Wound healing - a literature review. *Anais Brasileiros de Dermatol.* **91**, 614–620 (2016).
11. Derwin, R., Patton, D., Strapp, H. & Moore, Z. Wound pH and temperature as predictors of healing: an observational study. *J Wound Care* **32**, 302–310 (2023).
12. Rauscher, M. et al. Influence of accumulation of humidity under wound dressings and effects on transepidermal water loss (TEWL) and skin hydration. *Appl. Sci.* **14**, 7739 (2024).
13. Ukaegbu, K., Allen, E. & Svoboda, K. K. H. Reactive oxygen species and antioxidants in wound healing: mechanisms and therapeutic potential. *Int. Wound J.* **22**, https://doi.org/10.1111/iwj.70330 (2025).
14. Wang, G. et al. The initiation of oxidative stress and therapeutic strategies in wound healing. *Biomed. Pharmacotherapy* **157**, 114004 (2023).
15. Tang, X., Yang, T., Yu, D., Xiong, H. & Zhang, S. Current insights and future perspectives of ultraviolet radiation (UV) exposure: Friends and foes to the skin and beyond the skin. *Environ. Int.* **185**, 108535 (2024).
16. Eming, S. A., Martin, P. & Tomic-Canic, M. Wound repair and regeneration: Mechanisms, signaling, and translation. *Sci. Transl. Med.* **6**, https://doi.org/10.1126/scitranslmed.3009337 (2014).
17. Tan, J. L. et al. Restoration of the healing microenvironment in diabetic wounds with matrix-binding IL-1 receptor antagonist. *Commun. Biol.* **4**, 422 (2021).
18. Kruse, C. R. et al. The external microenvironment of healing skin wounds. *Wound Repair Regen.* **23**, 456–464 (2015).
19. Wang, Z., Qi, F., Luo, H., Xu, G. & Wang, D. Inflammatory Microenvironment of Skin Wounds. *Front. Immunol.* **13**, https://doi.org/10.3389/fimmu.2022.789274 (2022).
20. Kumar, P. et al. Role of angiogenesis and angiogenic factors in acute and chronic wound healing. *Plast Aesthet Res.* **2**, 243 (2015).
21. Veith, A. P., Henderson, K., Spencer, A., Sligar, A. D. & Baker, A. B. Therapeutic strategies for enhancing angiogenesis in wound healing. *Adv. Drug Deliv. Rev.* **146**, 97–125 (2019).
22. Guillamat-Prats, R. The role of MSC in wound healing, scarring and regeneration. *Cells* **10**, 1729 (2021).
23. SCHAFER, M. & Werner, S. Oxidative stress in normal and impaired wound repair. *Pharmacol. Res.* **58**, 165–171 (2008).
24. Fadilah, N. I. M. et al. Antioxidant biomaterials in cutaneous wound healing and tissue regeneration: a critical review. *Antioxidants* **12**, 787 (2023).
25. Kim, J. H. et al. High levels of oxidative stress and skin microbiome are critical for initiation and development of chronic wounds in diabetic mice. *Sci Rep* **9**, 19318 (2019).
26. Hunt, M., Torres, M., Bachar-Wikstrom, E. & Wikstrom, J. D. Cellular and molecular roles of reactive oxygen species in wound healing. *Commun. Biol.* **7**, 1534 (2024).
27. Dhivya, S., Padma, V. V. & Santhini, E. Wound dressings - a review. *BioMedicine.* **5**, https://doi.org/10.7603/s40681-015-0022-9 (2015).
28. Nuutila, K. & Eriksson, E. Moist wound healing with commonly available dressings. *Adv. Wound Care* **10**, 685–698 (2021).
29. Weller, C. D., Team, V. & Sussman, G. First-line interactive wound dressing update: a comprehensive review of the evidence. *Front. Pharmacol.* **11**, https://doi.org/10.3389/fphar.2020.00155 (2020).
30. Hodge, J. G., Zamierowski, D. S., Robinson, J. L. & Mellott, A. J. Evaluating polymeric biomaterials to improve next generation wound dressing design. *Biomater. Res.* **26**, https://doi.org/10.1186/s40824-022-00291-5 (2022).
31. Pang, Q. et al. Smart wound dressing for advanced wound management: real-time monitoring and on-demand treatment. *Mater Des* **229**, 111917 (2023).
32. Gupta, A., Avci, P., Dai, T., Huang, Y.-Y. & Hamblin, M. R. Ultraviolet radiation in wound care: sterilization and stimulation. *Adv Wound Care* **2**, 422–437 (2013).
33. Horton, L., Brady, J., Kincaid, C. M., Torres, A. E. & Lim, H. W. The effects of infrared radiation on the human skin. *Photodermatol. Photoimmunol. Photomed.* **39**, 549–555 (2023).
34. Gou, Y., Hu, L., Liao, X., He, J. & Liu, F. Advances of antimicrobial dressings loaded with antimicrobial agents in infected wounds. *Front. Bioeng. Biotechnol.* **12**, https://doi.org/10.3389/fbioe.2024.1431949 (2024).
35. Nejaddehbashi, F. et al. Antibacterial and antioxidant double-layered nanofibrous mat promotes wound healing in diabetic rats. *Sci Rep* **13**, 3166 (2023).
36. Raman, A. P., Anoma, M. A., Zhu, L., Rephaeli, E. & Fan, S. Passive radiative cooling below ambient air temperature under direct sunlight. *Nature* **515**, 540–544 (2014).
37. Bhatia, B. et al. Passive directional sub-ambient daytime radiative cooling. *Nat Commun* **9**, 5001 (2018).
38. Zhou, L. et al. Radiative cooling for energy sustainability: Materials, systems, and applications. *Phys. Rev. Mater.* **6**, 090201 (2022).
39. Li, Z., Chen, Q., Song, Y., Zhu, B. & Zhu, J. Fundamentals, materials, and applications for daytime radiative cooling. *Adv. Mater. Technol.* **5**, https://doi.org/10.1002/admt.201901007 (2020).
40. Zhao, D. et al. Radiative sky cooling: fundamental principles, materials, and applications. *Appl. Phys. Rev.* **6**, https://doi.org/10.1063/1.5087281 (2019).
41. Liang, J. et al. Radiative cooling for passive thermal management towards sustainable carbon neutrality. *Natl. Sci. Rev.* **10**, https://doi.org/10.1093/nsr/nwac208 (2023).
42. Mousavi, N. S. S. & Azzopardi, B. Perspectives on the applications of radiative cooling in buildings and electric cars. *Energies* **16**, 5256 (2023).
43. Wu, R. et al. *Spectrally Engineered Textile for Radiative Cooling against Urban Heat Islands*. https://www.science.org.
44. Kang, M. H. et al. Outdoor-useable, wireless/battery-free patch-type tissue oximeter with radiative cooling. *Adv. Sci.* **8**, 2004885 (2021).
45. Zhang, X. et al. Advanced cooling textiles: mechanisms, applications, and perspectives. *Adv. Sci.* **11**, https://doi.org/10.1002/advs.202305228 (2024).
46. Zhang, Q. et al. Daytime radiative cooling dressings for accelerating wound healing under sunlight. *Nat. Chem. Eng.* **1**, 301–310 (2024).
47. Teodorescu, M., Bercea, M. & Morariu, S. Biomaterials of poly(vinyl alcohol) and natural polymers. *Polym. Rev.* **58**, 247–287 (2018).
48. Marin, E., Rojas, J. & Ciro, Y. A review of polyvinyl alcohol derivatives: promising materials for pharmaceutical and biomedical applications. *Afr. J. Pharm. Pharmacol. Rev.* **8**, 674–684 (2014).
49. Gajra, B. et al. Poly vinyl alcohol hydrogel and its pharmaceutical and biomedical applications: a review. *Int. J. Pharm. Res.* **4**, 20–23 (2012).
50. Reim, M. et al. Silica-aerogel granulate - structural, optical and thermal properties. *J. Non Crystal. Solids* **350**, 358–363 (2004).
51. Mandal, J. et al. Hierarchically porous polymer coatings for highly efficient passive daytime radiative cooling. *Science* **362**, 315–319 (2018).
52. Zhang, D., Zhang, H., Xu, Z. & Zhao, Y. Recent advances in electrospun membranes for radiative cooling. *Materials* **16**, https://doi.org/10.3390/ma16103677 (2023).
53. Kou, J., Jurado, Z., Chen, Z., Fan, S. & Minnich, A. J. Daytime radiative cooling using near-black infrared emitters. *ACS Photonics* **4**, 626–630 (2017).
54. Ding, Z. et al. Robust radiative cooling via surface phonon coupling-enhanced emissivity from SiO_2 micropillar arrays. *Int. J. Heat Mass Transf.* **220**, 125004 (2024).
55. Huang, X., Ge, X., Zhou, L. & Wang, Y. Eugenol embedded zein and poly(lactic acid) film as active food packaging: formation, characterization, and antimicrobial effects. *Food Chem.* **384**, 132482 (2022).
56. Liu, Z. et al. Superhydrophobic and highly moisture-resistant PVA@EC composite membrane for air purification. *RSC Adv.* **12**, 34921–34930 (2022).
57. Cui, C. et al. Hydrophobic biopolymer-based films: strategies, properties, and food applications. *Food Eng. Rev.* **15**, 360–379 (2023).
58. Safari, R., Amiri, R. Z. & Esmaeilzadeh Kenari, R. Antioxidant and antibacterial activities of C-phycocyanin from common name Spirulina platensis. *Iran J. Fish Sci.* **19**, 1911–1927 (2020).
59. Bannu, S. M. et al. Potential therapeutic applications of C-phycocyanin. *Curr Drug Metab* **20**, 967–976 (2019).
60. Fernandes, R. et al. Exploring the benefits of phycocyanin: from spirulina cultivation to its widespread applications. *Pharmaceuticals* **16**, 592 (2023).
61. Refai, H. et al. Enhanced wound healing potential of Spirulina platensis nanophytosomes: metabolomic profiling, molecular networking, and modulation of HMGB-1 in an excisional wound rat model. *Mar Drugs* **21**, 149 (2023).
62. Madhyastha, H. K., Radha, K. S., Nakajima, Y., Omura, S. & Maruyama, M. uPA dependent and independent mechanisms of wound healing by C-phycocyanin. *J. Cell Mol. Med.* **12**, 2691–2703 (2008).
63. Zhu, H. et al. Electrospun poly(vinyl alcohol)/silica film for radiative cooling. *Adv Compos Hybrid Mater.* **5**, 1966–1975 (2022).
64. Lee, D., Kwon, S. & Kim, M. ViBA Rad: visualization and basic analysis tools for radiative cooling. *SoftwareX* **24**, 101562 (2023).
65. McNichol, L., Lund, C., Rosen, T. & Gray, M. Medical adhesives and patient safety: State of the science consensus statements for the assessment, prevention, and treatment of adhesive-related skin injuries. *J. Wound Ostomy Continence Nurs.* **40**, 365–380 (2013).
66. Linz, M. S., Mattappallil, A., Finkel, D. & Parker, D. Clinical impact of Staphylococcus aureus skin and soft tissue infections. *Antibiotics* **12**, 557 (2023).

67. Monk, E. J. M. et al. Antimicrobial resistance in bacterial wound, skin, soft tissue and surgical site infections in Central, Eastern, Southern and Western Africa: a systematic review and meta-analysis. *PLOS Global Public Health* **4**, e0003077 (2024).
68. Galiano, R. D., Michaels V, J., Dobryansky, M., Levine, J. P. & Gurtner, G. C. Quantitative and reproducible murine model of excisional wound healing. *Wound Repair Regen.* **12**, 485–492 (2004).
69. Chen, Z. et al. Differential distribution and genetic determination of eccrine sweat glands and hair follicles in the volar skin of C57BL/6 mice and SD rats. *BMC Vet Res.* **18**, 316 (2022).
70. Sun, G. et al. Dextran hydrogel scaffolds enhance angiogenic responses and promote complete skin regeneration during burn wound healing. *Proc. Natl. Acad. Sci. USA* **108**, 20976–20981 (2011).
71. Smallcombe, J. W. et al. Quantifying the impact of heat on human physical work capacity; part IV: interactions between work duration and heat stress severity. *Int. J. Biometeorol.* **66**, 2463–2476 (2022).
72. Abràmoff, M. D., Magalhães, P. J. & Ram, S. J. Image processing with imageJ. *Biophotonics Int.* **11**, https://doi.org/10.1201/9781420005615.ax4 (2004).